

# Dynamics of Triplet-State Photochemistry of Pentanal: Mechanisms of Norrish I, Norrish II, and H Abstraction Reactions

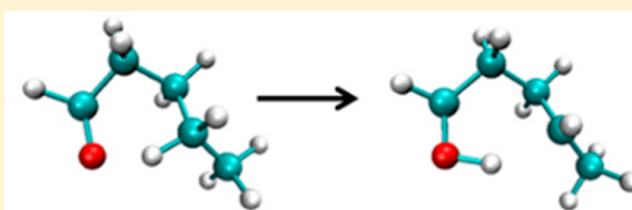
Dorit Shemesh,<sup>\*,†</sup> Zhenggang Lan,<sup>\*,‡</sup> and R. Benny Gerber<sup>\*,†,§</sup>

<sup>†</sup>Department of Physical Chemistry and the Fritz Haber Center for Molecular Dynamics, The Hebrew University, Jerusalem 91904, Israel

<sup>‡</sup>Key Laboratory of Biobased Materials and the Qingdao Key Lab of Solar Energy Utilization and Energy Storage Technology, Qingdao Institute of Bioenergy and Bioprocess Technology, Chinese Academy of Sciences, Qingdao 266101, China

<sup>§</sup>Department of Chemistry, University of California—Irvine, Irvine, California 92697, United States

**ABSTRACT:** The photochemistry of aldehydes in the gas phase has been the topic of extensive studies over the years. However, for all but the smallest aldehydes the dynamics of the processes is largely unknown, and key issues of the mechanisms are open. In this article, the photochemistry of pentanal is studied by dynamics simulation using a semiempirical MRCI code for the singlet and triplet potential energy surfaces involved. The simulations explore the processes on the triplet state following intersystem crossing from the initially excited singlet. Test simulations show that the photochemistry takes place on the adiabatic triplet surface only and that no nonadiabatic transitions occur to the other triplets. The main findings include the following: (1) Norrish type I and type II reactions and H detachment have been observed. (2) The time scales of Norrish type I and Norrish type II reactions are determined: Norrish type I reaction tends to occur in the time scale below 10 ps, whereas the Norrish type II reaction is mostly pronounced after 20 ps. The factors affecting the time scales are analyzed. (3) The relative yield for Norrish type I and type II reactions is 34% and 66%, which is close to the experimental observed ones. Bond orders and Mulliken partial charges are computed along the trajectories and provide mechanistic insights. The results throw light on the time scales and mechanisms and competition between different channels in aldehyde photochemistry. It is suggested that direct dynamics simulations using semiempirical potentials can be a very useful tool for exploring the photochemistry of large aldehydes, ketones, and related species.



## 1. INTRODUCTION

Aldehydes are ubiquitous in the atmosphere. One major source of aldehydes in the atmosphere results from biogenic emission, such as emission from biomass, living organisms, vegetation, etc. Other important sources are anthropogenic such as the incomplete combustion of petroleum fuels in the industry. Smaller alkyl aldehydes are also created in the atmosphere itself by photooxidation of hydrocarbons, ether, alcohols, and other organic compounds.

Aldehydes play a central role in the formation of photochemical smog,<sup>1</sup> peroxyacetyl nitrate (PAN), and ground state ozone. Removal of aldehydes from the atmosphere proceeds by reaction with OH radicals and unimolecular photodissociation. As a result, they constitute a source of free radicals in the lower atmosphere, which influences the atmospheric oxidation capacity.<sup>2–4</sup> It is therefore of major interest to understand the mechanistic picture of their photodissociation and especially their contribution to radical formation.

Aliphatic aldehydes exhibit a weak absorption band in the wavelength range 240–360 nm as a result of a dipole forbidden  $n \rightarrow \pi^*$  transition.<sup>5,6</sup> Photolysis of aldehydes can possibly occur through the following pathways:



Process 1 is the molecular fragmentation channel. Process 2 represents the fragmentation into free radicals (Norrish type I reaction). In principle, the hydrogen of the HCO radical can further be transferred to the other fragment in a second step, yielding CO and an alkane as a product. Process 3 is called Norrish type II reaction. Process 4 is an H abstraction process and has been found to be minor in small aldehydes.<sup>7</sup> In the microscopic picture, the photoexcitation promotes the system to the first singlet state ( $S_1$ ) of  $n\pi^*$  character. Then, the  $S_1$  state can either switch to the ground  $S_0$  state via internal conversion or reach the triplet state via intersystem crossing. There is evidence that process (2) can occur either on the ground state or on the triplet state.<sup>8</sup>

**Special Issue:** Curt Wittig Festschrift

**Received:** February 5, 2013

**Revised:** June 14, 2013

**Published:** June 17, 2013



Theoretical studies of the photochemistry of small aldehydes, particularly on their photodissociation via singlet and triplet states, cover both electronic–structure calculations and non-adiabatic-dynamics simulations.<sup>9,10</sup> Even small aldehydes can exhibit complex mechanisms, for example, roaming of a hydrogen around the rest of the system in formaldehyde<sup>11</sup> and H/D scrambling for acetaldehyde.<sup>12,13</sup>

Because of higher computational cost, theoretical studies on photodissociation of larger aldehydes mostly focus on important structures (minima, transition states, and conical intersections) and on possible reactions pathways.<sup>14–16</sup> So far, most studies of aldehydes larger than four carbon atoms have been of experimental nature. A systematic theoretical study using a dynamical approach to the photodissociation of medium-sized and large aldehydes is therefore of major interest for understanding the detailed mechanism of the process.

Systematic experimental work has been performed to study the influence of the chain length on the photolysis of aldehydes (from small aldehydes up to octanal).<sup>7–9,11–32</sup> It is generally accepted that small aldehydes up to the size five carbon atoms prefer to dissociate exclusively according to Norrish type I reaction, but for larger ones, Norrish type II reactions play the main role. This has been already stated in the book of Calvert and Pitts<sup>5</sup> and has been confirmed by extensive experiments in this area, see, for example, refs 7–9, 11–13, and 15–32. The abbreviation of Cn will denote an aldehyde of the chain length *n*. The review article by Zhu et al.<sup>29</sup> summarizes the HCO yield of aldehydes in the size between C3 and C7. For C3, the peak quantum yield for HCO formation is almost 1. This drops rapidly for C4 (0.8) and becomes almost constant for C5 to C7 (between 0.2 and 0.15). This is explained by the opening of Norrish type II reaction at the size of four carbon atoms. The drop in quantum yield for aldehydes with at least five atoms is explained by the existence of secondary  $\gamma$ -hydrogen atoms, which are much more reactive than primary  $\gamma$ -hydrogen atoms in aldehydes of four carbon atoms. It can be seen from this review that, for aldehydes larger than four atoms, Norrish I and Norrish II are competitive and that the yield for Norrish I rapidly drops for systems of five or more carbon atoms.

All previous research suggests that pentanal is a very important case since it seems to be the turnover point between Norrish type I and Norrish type II reactions. The conclusions of the experimental studies on pentanal depends on the isomer of pentanal studied: A first study investigated the photodissociation of *i*-pentanal and *t*-pentanal by dye laser photolysis in combination with cavity-ring down spectroscopy. Here, the Norrish type I reaction is favored with a relative HCO yield of 92% for *t*-pentanal and 40% for *i*-pentanal,<sup>27</sup> with respect to Norrish type II reaction. The relative yield of HCO is lower for *i*-pentanal because of the presence of the Norrish type II channel. The author states that for *t*-pentanal the Norrish type II reaction is not possible, due to the structure of this isomer. Another experimental study using dye-laser photolysis of *n*-pentanal showed a different result, that Norrish type II reaction is the major dissociation channel (relative yield of 80%).<sup>25</sup> The third study investigated the photolysis of *n*-pentanal by fluorescent UV lamps in air at 298 K.<sup>28</sup> At 700 Torr, the Norrish type II reaction is preferred by a relative yield of 80%. From these studies, it can be seen that different isomers of pentanal and different experimental conditions result in different quantum yields between Norrish I and Norrish II reaction products. Thus, to address the detailed reaction mechanism, it is important to investigate the ratio between both

types of reactions theoretically using a molecular dynamics approach.

In this article, the excited-state dynamics of *n*-pentanal is investigated. The objectives of this study are as follows.

First, this study aims to understand the photochemistry of pentanal from first-principles using a reliable potential energy surface. In particular, the investigation of the mechanisms of the different reaction pathways involved is pursued. The relative role of Norrish type I and type II and non-Norrish reactions will be determined. Especially the study aims at checking whether for this system the threshold for contributions from Norrish II mechanism is realized. On the basis of this framework, the conditions that lead to Norrish II mechanism are proposed.

Second, the study aims at examining whether different triplet states play a role in the excited-state dynamics or if the photochemistry takes place on a single triplet surface. It should be noted that in principle there is a competition between the Norrish reactions on the singlet state and on the triplet states, as also stated in refs 14 and 26, for example. However, this study focuses on the mechanisms and time scales of the possible photochemical reactions on the triplet state surface.

In addition to establishing the photochemistry of pentanal and its underlining reaction mechanisms, this article also has a third, methodological, objective. A dynamical approach here as a computational tool for describing photochemistry of even larger aldehyde systems, possible also in the presence of a solvent environment, is suggested. In brief, an important objective here is to introduce an approach for photochemical simulations of large aldehydes.

The structure of the article is as follows: section II gives a more detailed description of the methodology used. Results are given in section III. Finally, conclusions are derived and presented in section IV.

## 2. METHODOLOGY

The current work focuses on the possible ultrafast excited-state dynamics of pentanal after photoexcitation. Several critical geometries, such as the ground-state, singlet, and triplet excited-state minima, were optimized. The excited-state potential-energy surfaces were discussed. Afterward, the on-the-fly adiabatic and nonadiabatic molecular dynamics were performed to understand molecular motion of pentanal on its low-lying singlet and triplet excited states. For nonadiabatic dynamics, the trajectory surface-hopping approach with Tully's fewest-switches algorithm was used. Through all calculations, the semiempirical OM2/MRCI method was applied in electronic-structure calculations. Some high-level methods, such as ADC(2), were taken for validation purposes. Next we try to address each step one by one.

**2.1. Spectroscopic Validation of OM2, OM2/MRCI, and ADC(2).** In the direct dynamics approach, the potential energy surface evaluation is the major time-consuming step. Preferably high level ab initio potentials should be chosen for this purpose, while for large systems this is not always feasible to do. Feasible simulation times can be obtained by using force fields. However, a major drawback of ordinary force fields is the inability to treat bond cleavage and creation due to the modeling of chemical bonds. The alternative approach is to employ semiempirical methods in which parameters are introduced for certain electronic integrals.

Our group has in the past successfully applied the PM3 semiempirical methods for various dynamical simulations, such

as photoionization dynamics of biological molecules,<sup>33–36</sup> overtone excitation in atmospherically relevant systems<sup>37,38</sup> and vibrational excitations in small peptides.<sup>39,40</sup> Very recently, semiempirical methods have been transferred to a GPU based computing platform.<sup>41</sup> The overall time usage is accelerated by 1 order of magnitude. This opens the possibility for treating much larger systems, in particular reactive ones, using semiempirical methods.

One successor to PM3 is OM2, namely, Orthogonalization corrected semiempirical Method 2. OM2 provides orthogonalization corrections for improving well-known semiempirical methods such as PM3. The advantage of OM2 over other semiempirical methods is that the excited states can then be treated by their equivalent excited state method, OM2/MRCI. This enables the treatment of possible excited-state dynamics, including transitions between different states.

The OMx potentials have been recently tested for thermochemistry, kinetics, and noncovalent interactions.<sup>42</sup> The main conclusion reached from this benchmark study for the ground-state potential is that these methods are almost as accurate and robust as DFT-GGA methods for organic molecules. Many previous studies have also proven that the OM2/MRCI method provide a reasonable description of excited-state processes of polyatomic organic molecules, for instance, nucleobases,<sup>43–49</sup> butadiene,<sup>50</sup> retinal model systems,<sup>51</sup> and the rhodopsin chromophore.<sup>52</sup> The recent benchmark studies have also shown the good performance of the OM2/MRCI, see refs 49 and 53–56 for details. The orthogonalization-corrected OM2 Hamiltonian<sup>57</sup> and the GUGA-CI approach<sup>58</sup> were employed to calculate the required energies, gradients, and nonadiabatic coupling vectors of electronic states. The restricted-open Hartree–Fock formalism was employed in the self-consistent-field calculations since this approach gives a better description of molecular singlet and triplet excited states. In GUGA-MRCI calculations, three reference configurations were used (closed shell and single and double HOMO–LUMO excitations). The active space was chosen to include the highest 5 occupied orbitals and the lowest 5 unoccupied orbitals for the pentanal molecule. The active space for pentanal was chosen based on comparison to the orbital excitations in ADC(2) calculations.

Semiempirical methods are capable of a qualitatively good description of the system with enormous time savings in the simulation process. Quantitatively, the semiempirical potentials are less accurate. It is therefore advisable to validate each system against higher level ab initio methods. This has also been done in this study. In particular, MP2 is used for comparison for ground state geometries and energies, ADC(2) for excited state structures and various excited state energies. It has been shown that OM2/MRCI and ADC(2) give comparable results. For more details, the reader is referred to the results section.

The structure of pentanal was optimized in the singlet ground state with MP2 in conjunction with the resolution-of-the-identity (RI) approximation<sup>59</sup> for the evaluation of the electron-repulsion integrals implemented in Turbomole.<sup>60</sup> Excitation energies were calculated by the ADC(2) method<sup>61</sup> implemented in Turbomole. The cc-pVDZ basis set has been employed.<sup>62</sup> ADC(2) has been successfully applied to various systems for predicting reaction profiles in organic systems.<sup>63–66</sup> The accuracy in some cases is extremely precise.<sup>67</sup> Recent developments of ADC(2) has been done, for example, in the group of Dreuw: implementation of unrestricted ADC(2),<sup>68</sup> its

application to several systems,<sup>69,70</sup> and the implementation of the calculation of nonlinear response properties.<sup>71</sup>

It is believed that the OM2 and OM2/MRCI potential can model qualitatively correctly the photoinduced dynamics of pentanal. Although this system can be still treated by higher level ab initio potentials, the goal is to extend this study in the future for clusters of aldehydes and solvated aldehydes. Those systems are considered too large for the treatment with high level ab initio potentials. Indeed, preliminary results on pentanal clusters show that the OM2 based potentials are very promising.

**2.2. Simulation of Photoinduced Processes in Pentanal.** Excited state dynamics calculations were performed with the semiempirical MNDO program.<sup>72,73</sup>

Figure 1 shows a schematic picture of the simulation approach. The sequence of the involved steps is denoted by numbers.

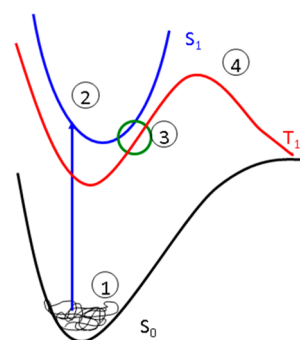


**Figure 1.** Schematic picture of the simulation approach. Numbers denote the sequence of the steps involved. (1) MD simulation on the ground state. (2) Vertical excitation of selected geometries and dynamics on the singlet excited state. (3) Assumption of intersystem crossing at the smallest singlet–triplet gap. (4) Dynamics on the triplet ground state (with and without nonadiabatic transitions).

The sequence of the steps of the simulation is described here. Below, more information is given for each individual step. First, the sampling to determine the initial conditions for the dynamics simulation is performed. These are the configurations on  $S_0$  from which vertical excitation to  $S_1$  in the spirit of the Franck–Condon excitation takes place. The second step then involves dynamics on the singlet  $S_1$  excited state. In the third step, geometries with small singlet–triplet gaps are chosen and are used as initial conditions for the dynamics on triplet states.

In this study, the same methodology for the photoexcitation dynamics as used previously in peroxide on the ice system is applied,<sup>55</sup> with additional simulations running on the triplet surface.

#### 2.2.1. Ground State MD Simulation and Initial Sampling.

The initial configurations were sampled by applying the selection criteria described below (see ref 74 for more details) to a large number of geometries obtained from a preliminary ground-state Born–Oppenheimer molecular dynamics simulation. Two criteria were used for selecting the initial structures for nonadiabatic dynamics simulations. First, the vertical excitation energy of pentanal must be in a range of  $\pm 0.6$  eV from the vertical excitation energy at the reference geometry ( $S_0$  minimum of pentanal). In principle, excitation to all states is possible, but the energy window limits the excitation in this case to the first excited state only. Second, geometries are



selected by considering their transition probability. The relative transition probability is calculated by (see ref 75)

$$P = \frac{\left(\frac{f}{\Delta E}\right)}{\max\left(\frac{f}{\Delta E}\right)} = \frac{|\mu|^2}{\max(|\mu|^2)} \quad (5)$$

where  $f$  is the oscillator strength,  $\Delta E$  is the energy gap between the states, and  $\mu$  is the transition dipole moment. For each state, a random number  $0 < n < 1$  is generated, and if  $n < P$ , then the structure is accepted. By this procedure, 70 initial structures were selected and vertically put on the first singlet excited-state, S1, for starting of the photoexcited dynamics simulations.

**2.2.2. Dynamics on the Singlet Excited States.** From the first singlet excited-state, S1, nonadiabatic surface hopping dynamics were performed. The adiabatic dynamics only considered the dynamics in the lowest singlet excited state. For nonadiabatic surface hopping dynamics, the ground state and two excited states were included. The adiabatic representation was used in all the calculations. Nuclear degrees of freedom were propagated along classical trajectories with a time step of 0.1 fs using the velocity-Verlet algorithm.

The time evolution of quantum amplitudes for electronic motions was calculated using a unitary propagator and a time step 200 times smaller. The hopping probability was computed by the Tully's fewest switches algorithm.<sup>76</sup> A set of 27 trajectories were propagated for 450 fs using nonadiabatic surface hopping dynamics. No interesting events (such as S1–S0 transitions or bond dissociation) happened in these trajectories. All trajectories display similar features, and they are trapped near S1 minimum. Furthermore, a test nonadiabatic surface hopping trajectory for about 17 ps was run to check whether reactions occur on a longer time scale, and no reactions were found. Thus, within the simulation time, no ultrafast S1–S0 decay and bond dissociation are observed. Since the system can stay in S1 state quite long, this may allow the opening of the intersystem crossing channel from the singlet to triplet states. This is consistent with the experimental observations that confirmed the essential role of triplet state in the photodissociation dynamics of aldehydes.<sup>8</sup>

**2.2.3. Intersystem Crossing Assumption.** Nonadiabatic transitions can take place between the electronic states with different multiplicities, and such intersystem crossing process is induced by spin–orbital couplings. In some cases, ultrafast spin-flip has been observed experimentally and theoretically.<sup>77,78</sup> Very recently, ultrafast spin flip has been observed theoretically using on-the-fly simulations for the  $\text{Cl} + \text{O}_3 \rightarrow \text{ClO} + \text{O}_2$  reaction.<sup>79</sup> The theoretical treatments of ultrafast intersystem crossing have also aroused research interests. In principle, it is possible to treat the ISC event rigorously, as has been done by Krylov,<sup>80</sup> Marian,<sup>81,82</sup> and Gonzalez.<sup>83,84</sup> For instance, the new program SHARC includes a reformulation of surface hopping dynamics that allows to treat interactions such as spin–orbit coupling or transitions induced by laser fields.<sup>83</sup> Most of the above-mentioned methodology employs Tully's nonadiabatic surface hopping dynamics<sup>76</sup> in conjunction with different potential energy surfaces. Tully's nonadiabatic surface hopping dynamics has been evolved to the state of the art method for treating nonadiabatic transitions for polyatomic systems.

For many organic compounds, the spin-flip dynamics is in general not ultrafast (time scale of ISC is in the order of  $10^{-8}$  s)

due to the weak spin–orbit couplings.<sup>5</sup> Previous work suggested that the triplet states should be responsible for photochemistry of aldehydes.<sup>8</sup> Thus, it should be reasonable to assume that pentanal also exhibits intersystem crossing. However, such slow process cannot be simulated directly by dynamical approach due to high computational costs of on-the-fly electronic–structure calculations and possible deficiency of surface-hopping method. It is beyond the scope of this article to simulate the intersystem crossing event itself. Since one of the main focuses of this study is the ultrafast dynamics on the triplet states, it is only necessary to address the suitable initial conditions for such dynamics. For this purpose, a simplified model for intersystem crossing was used, which assumed that the intersystem crossings happen only at those geometries with small singlet–triplet energy gaps. These geometries should give the reasonable starting conditions for the following dynamics on triplet states. Although not rigorous, such approach should be accepted since the main purpose is to understand the dynamics on triplet states instead of the intersystem crossing event. In practice, the singlet–triplet energy difference along several trajectories propagating on the S1 state is calculated. From each trajectory, two geometries having the lowest singlet–triplet energy difference (ranging from 0.23 to 0.29 eV) are chosen. It is assumed that the intersystem crossing happens at these geometries. Then, these geometries were used as the initial conditions for the dynamics on the triplet state. A similar approach has also been widely used to investigate the dynamics starting from conical intersection or the top of reaction barrier on the excited states.<sup>85,86</sup>

**2.2.4. Triplet State Dynamics.** We then started to run from these geometries trajectories on the triplet state, both adiabatic dynamics and dynamics allowing nonadiabatic transitions. To examine the dependence of reaction dynamics on initial kinetic energy, two different situations were considered. Since the intersystem-crossing should take place around the order of  $10^{-8}$  s that is slower than vibrational relaxation, the thermal equilibrium is achieved after the system jumps to the triplet state. Thus, it should be reasonable to generate the initial velocity of each atom by Monte Carlo sampling of kinetic energy that can be converted to equivalent temperature (200 and 300 K). Adiabatic dynamics on the lowest triplet state and nonadiabatic dynamics involving three lowest triplet states both last 10 ps. For each set, 54 trajectories were employed.

Additionally, long time scale simulations have been performed using the same initial structures with different random velocities (equivalent to a temperature of 300 K) for a set of 108 trajectories for a time scale of 100 ps. The difference in the samples is referred by using the terms short time scale simulations (up to 10 ps) and long time scale simulations (up to 100 ps).

Final results were obtained by averaging over 54 (108 for the long time scale simulation) trajectories for the pentanal molecule.

The cleavage distance for the C–C $_{\alpha}$  bond breaking was defined as 2.5 Å. At this distance, the chemical interaction between the fragments is negligible. The percentage of dissociation events at a specific time was defined as the number of trajectories that dissociates at this time divided by the total number of trajectories that show dissociation. Additional insight into several reactions is gained by calculating the bond order<sup>87</sup> and the Mulliken charges along the trajectories using the MNDO program. A similar approach has been recently used by Hirshberg et al. in analyzing the decomposition mechanisms and dynamics of N<sub>6</sub>.<sup>88</sup>

Finally, additional insight about the energetics has been gained by calculating minimum energy paths between initial and final geometries. In all the minimum energy paths shown here, one coordinate was kept frozen, and all the other coordinates were allowed to vary freely.

### 3. RESULTS AND DISCUSSION

**3.1. Structure and Vertical Excitation Energy.** Pentanal has been optimized with RI-MP2. The structure is shown in Figure 2.

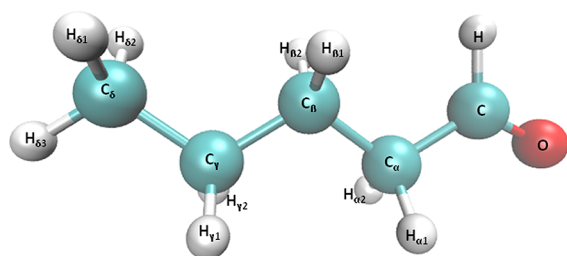


Figure 2. Optimized geometry of pentanal.

Optimization with OM2/MRCI leads to a similar structure. To our knowledge, there exists no study on possible conformers of pentanal. It is assumed that this structure presents the global minimum. All bent structures would result in more steric repulsion and would therefore heighten the energy.

Table 1 summarizes the vertical excitation energy as calculated by ADC(2). For comparison, Table 2 shows the

Table 1. ADC(2) Singlet Excitation Energy of Pentanal

state	energy (in eV)	oscillator strength	description	
1	4.11	0.00003	HOMO → LUMO	$n\pi^*$
2	8.14	0.106	HOMO → LUMO + 2	
			HOMO → LUMO + 3	
3	8.44	0.005	HOMO → LUMO + 1	

Table 2. OM2/MRCI Singlet Excitation Energy of Pentanal

state	energy (in eV)	oscillator strength	description	
1	3.76	0.002	HOMO → LUMO	$n\pi^*$ , same orbitals as in the ADC(2) excitation
2	6.14	0.231	HOMO → LUMO + 1	
3	8.09	0.068	HOMO - 1 → LUMO	$\pi\pi^*$
			HOMO - 4 → LUMO	

vertical excitation energy as calculated by OM2/MRCI. The first excitation with both methods corresponds to an  $n\pi^*$  transition. The same orbitals are involved in both methods and are shown in Figure 3.

Experimentally, the peak of transition observed lies at 4.20 eV and corresponds to an  $n\pi^*$  transition.<sup>28</sup> The first vertical excitation energy predicted by the ADC(2) is in excellent agreement with the experimental value. OM2/MRCI predicts a slightly smaller value than the experimental value but is still in quite good agreement. The next singlet excited state lies at least 2.5 eV higher above the first excited state and seems therefore not to be important in the photoexcitation dynamics. Overall, it is concluded that OM2/MRCI seems to describe

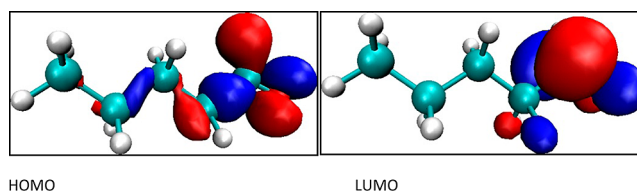


Figure 3. Orbitals from ADC(2) involved in the transition to the first singlet excited state.

qualitatively and quantitatively the first excited state correctly and is therefore a reliable potential for usage in the photoexcitation dynamics.

As will be seen below, the reactions are taking place on the triplet surface. Therefore, also the triplet excitation energies calculated by ADC(2) and OM2/MRCI are compared. Table 3 summarizes the triplet excitation energy.

Table 3. Triplet Excitation Energy of Pentanal Relative to the Optimized  $S_0$  State

state	ADC(2) energy (in eV)	OM2/MRCI energy (in eV)
T1	3.75	3.16
T2	5.44	5.14

Note, that the triplet excitation energies are calculated at the T1 optimized geometry.

As expected, the triplet excitation energy lies in both cases below the energy of the first singlet state. The energy difference between the first singlet state and the triplet state is about 0.5 eV. The OM2/MRCI triplet excitation energy is calculated about 0.5 eV below the ADC(2) energy. The same tendency has been seen for the first singlet excited state. The second triplet state lies between 1.5–2 eV higher than the first triplet state. It is assumed therefore that the higher triplet states do not play a role in the excitation dynamics. Overall, the OM2/MRCI energies are in qualitatively and quantitatively good agreement with the ADC(2) energies and the experiment. It is therefore expected that this holds also for the photoexcitation dynamics.

**3.2. Overview of Possible Reactions.** Figure 4 summarizes the reactions that are possible in this system, in particular those that are seen in these simulations.

Three different types of reaction are observed: (1) the first step in the Norrish type I reaction, namely, the cleavage of the C–C $_{\alpha}$  bond, is seen. (2) The first step of the Norrish type II reaction, a major reaction path in these simulations, is observed. (3) As a minor path, the H detachment is observed. In the following, the study focuses on each reaction pathway and provides mechanistic insight and time scales for these reactions.

**3.3. Excited-State Dynamics.** Test simulations were carried out to examine whether processes occur on a short time scale following excitation to S1. All the trajectories were run for 450 fs. There were no reactions taking place in the trajectories. All the trajectories stayed on the first singlet excited state; transition to another excited state or to the ground state did not occur. Additionally, a test run for about 17 ps to check for long time events was done. No reactions were found. Other, less systematic searches of the S1 potential surface, also do not suggest pathways for low energy reactions. It is therefore assumed that intersystem crossing occurs from the singlet to the triplet state and that the reactions are taking place on the triplet surface. This is also assumed in other relevant work on

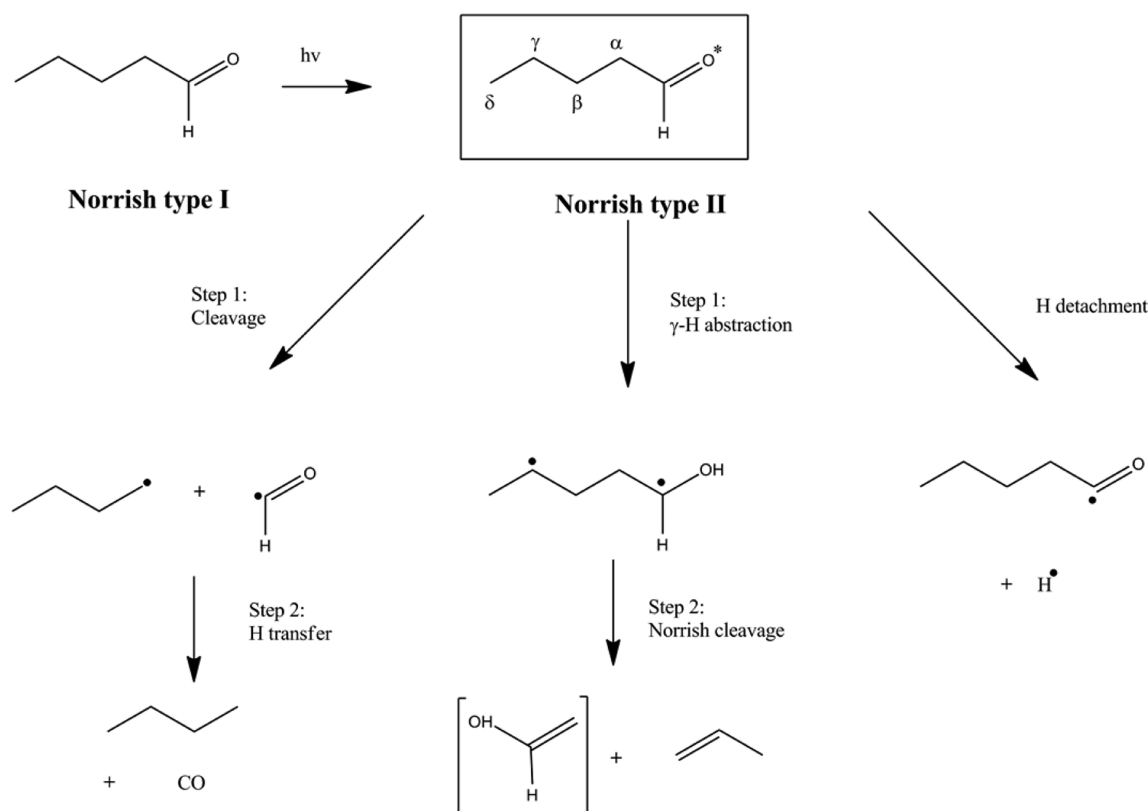


**Figure 4.** Schematic overview over possible reactions of pentanal.

photoexcitation dynamics of aldehydes, see, for example, ref 15. It should be emphasized that in principle reactions can take place also on the excited singlet state surface, as discussed in refs 14 and 26 and that the reaction channels on S1 is, in principle, competitive with those on the triplet state. However, there are barriers along both pathways on S1 state, see ref 26. The heights of the barriers for Norrish I and II on the S1 state are quite high. It is therefore assumed that no direct dissociation pathway exists on S1 state except via quantum tunnelling that takes place also at long time. At the same time, ISC may take place near the Franck–Condon region. Thus, the slow decay via quantum tunneling and ISC are competitive to each other. Therefore, it is possible that both reactions may take place, while the rate of them should also be very slow. The relative role of the T1 and S1 mechanisms probably depends on the relative time scales of tunneling versus ISC. However, from these simulations, we see that there are no reactions on S1 in the short time scale. This might be due to higher barrier, a longer distance from the Franck–Condon region to the transition states or other unknown effects. In this study, we therefore focus only on the triplet dynamics after ISC has occurred and discuss the mechanisms and the time scales of these reactions on the triplet surface. It is beyond the scope of this article to discuss the competition of the Norrish type I/II reactions channels on T1 vs S1.

**3.3.1. Short Time Scale Statistics.** The adiabatic dynamics on the lowest T state at 200 K (300 K) show that no reaction occurs in 91% (89%) of the trajectories. The remaining 10% show either C–C $_{\alpha}$  cleavage or other reactions, which will be analyzed in more detail in the next sections. Table 4 summarizes the statistics of different observed pathways at 200 and 300 K.

**Table 4. Percentage of Observed Reactions at  $T = 200$  and 300 K for the Time Scale of 10 ps**

pathway	percentage of observed reactions at temperature	
	200 K	300 K
C–C $_{\alpha}$ cleavage	7%	9%
$\gamma$ -H transfer	2%	0%
H detachment	0%	2%

Obviously, only a minor fraction of the pathways are reactive. This suggests that the typical time scale for the reactions is much longer than the simulation time of 10 ps employed in this study. This limited number of reactive events can therefore not be used to predict the overall statistics of the reactions. However, for understanding the mechanistic picture of the reactions, even a few reactive events are enough. The detailed dynamics of these events is therefore analyzed.

**3.3.2. Long Time Scale Statistics.** The long time scale statistics differ much from the short time scale statistics. Table 5 summarizes the percentage of observed reactions.

**Table 5. Percentage of observed reactions at  $T = 300$  K for the time scale of 100 ps**

pathway	percentage of observed reactions
	300 K
C–C $_{\alpha}$ cleavage	14%
$\gamma$ -H transfer	27%
H detachment	1%

It can be clearly seen, that the percentage of the C–C $_{\gamma}$  cleavage and the  $\gamma$ -H transfer rises. More importantly, the  $\gamma$ -H

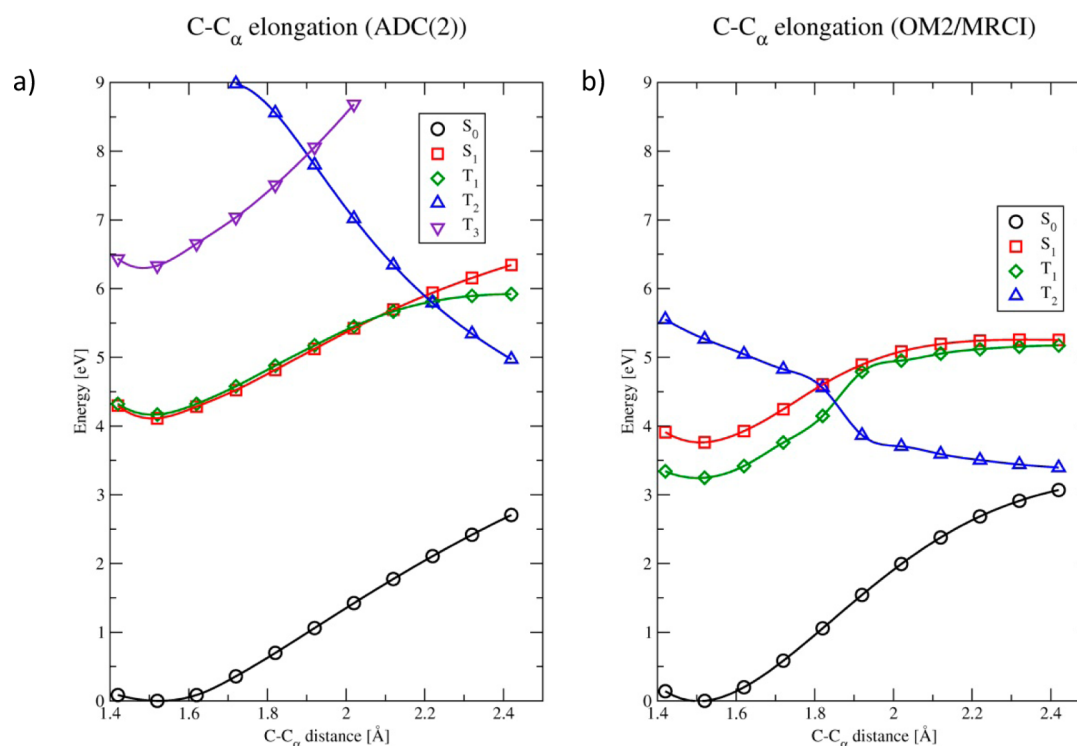


**Figure 5.** Potential energy surface along C–C<sub>α</sub> elongation calculated by (a) ADC(2) and (b) OM2/MRCI.

transfer channel clearly opens up in the longer time scale and is even the dominant process now. The relative yield of the Norrish type I reaction (C–C<sub>γ</sub> cleavage) is now 34% compared to the Norrish type II reaction (γ-H transfer) of 66%. The relative yield for Norrish type II of 66% obtained by the long time scale simulations now approaches the experimental relative yield of 80%.<sup>25,28</sup> More details on the time scales of the Norrish type I and II processes in the range up to 100 ps are given in section 3.8 after a detailed discussion on the mechanisms of these reactions.

### 3.4. Nonadiabatic Transitions between Triplet States.

The photodynamics of pentanal is known to take place on the triplet state surface. However, it has not been investigated so far, whether one triplet or several triplet states are involved in the photoinduced dynamics. In this study, this question is explicitly tested using nonadiabatic surface hopping dynamics between different triplet states. No transitions in all test runs that were performed have been observed. It is therefore concluded that the photoinduced dynamics of pentanal takes place only on the ground triplet state.

**3.5. Norrish Type I Reaction. 3.5.1. C–C<sub>α</sub> Bond Breaking: First Step in Norrish I.** One major reaction possible in pentanal is the Norrish type I reaction; see discussion in the introduction. The first step of Norrish type I is the C–C<sub>α</sub> breakage. The adiabatic energy along the C–C<sub>α</sub> elongation with ADC(2) and OM2/MRCI has been calculated. The potential energy profiles are plotted in Figure 5. Note that the vertical excitation energy of the triplet state in this figure refers to the energy of the triplet state at the geometries of the *optimized singlet state*. Therefore, this energy differs from the energy given in Table 3, where the *triplet state itself was optimized*.

For both methods, the C–C<sub>α</sub> breakage on the ground state involves a barrier of at least 3 eV. The S<sub>1</sub> state is shifted by about 4 eV from the ground state and shows the same tendency: about 3 eV must be invested for breaking this bond

on the first singlet excited state. Both methods predict the first triplet state below the first singlet state, and with ADC(2), these states are even almost degenerate. The closeness of these states points to a high coupling between these states, which can lead to intersystem crossing from S<sub>1</sub> to T<sub>1</sub>. Both methods predict another important state along the elongation of the C–C<sub>α</sub> bond. There is clearly a crossing between curves in Figure 5 (T<sub>2</sub> state crosses S<sub>1</sub> and T<sub>1</sub>). The location of the crossing of this state differs between both methods. The crossing is predicted to occur at a C–C<sub>α</sub> distance of about 2.2 Å for ADC(2) and at shorter distance (1.8 Å) for OM2/MRCI. Also, the energy of the T<sub>2</sub> state is predicted to be lower with OM2/MRCI than ADC(2). The energy difference between the T<sub>1</sub> minimum and the crossing is predicted to be 1.6 eV for ADC(2) and 1 eV for OM2/MRCI. Compared to the initial available energy (excitation to the S<sub>1</sub> state), the energy difference diminishes to 0.55 eV for OM2/MRCI level and stays approximately the same (1.7 eV) at the ADC(2) level. It is suggested that the dynamics does not perform in this case a nonadiabatic transition at the crossing geometry of Figure 5 because the system does not reach this configuration. The other coordinates do not correspond to the situation in the calculation of the figure. ADC(2) predicts another triplet state (T<sub>3</sub>). This state is predicted to be much higher in energy with OM2/MRCI and is therefore not plotted here. The orbital transitions describing these states are similar for both methods. Overall, the potential energy profile predicted by OM2/MRCI along the C–C<sub>α</sub> bond elongation is in qualitatively good agreement with the one predicted by ADC(2). The crossing between the states occurs at shorter C–C<sub>α</sub> distance, which might also affect the time scale of the dynamics.

From these profiles, it might be expected that more than one triplet state is significant for the photoexcitation dynamics. This can be easily verified by running photoexcitation dynamics with and without nonadiabatic surface hopping. As pointed out



already earlier, additional calculations using nonadiabatic surface hopping have been run. There are clearly no nonadiabatic transitions between different triplet states. It is therefore concluded that other triplet states are not relevant in the photo-induced dynamics of pentanal.

As mentioned above, strengthened also by Figure 3, it is assumed that the population is transferred from S1 to T1 by intersystem crossing. Structures from the singlet excited state dynamics (procedure described above), which have an energy difference between 0.23 to 0.29 eV between the S1 and the T1 state, have been extracted. The photoexcitation dynamics then proceeded from these structures on the T1 surface. In the next section, the results of the adiabatic triplet state dynamics are discussed.

### 3.5.2. Mechanistic Insight into the Norrish Type I Reaction: Partial Charges and Bond-Orders along Trajectories. Figure 6

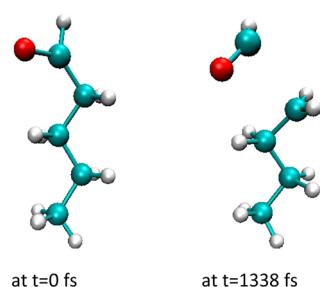


Figure 6. Snapshots of C–C<sub>α</sub> cleavage.

shows snapshots of the first step in the Norrish type I reaction seen in a typical trajectory. The mechanistic picture seems to be very simple: Upon accumulation of sufficient energy in the C–C<sub>α</sub> bond, the bond cleavage happens immediately.

In order to obtain more details of the mechanism, the bond order along a typical trajectory has been calculated; see Figure 7.

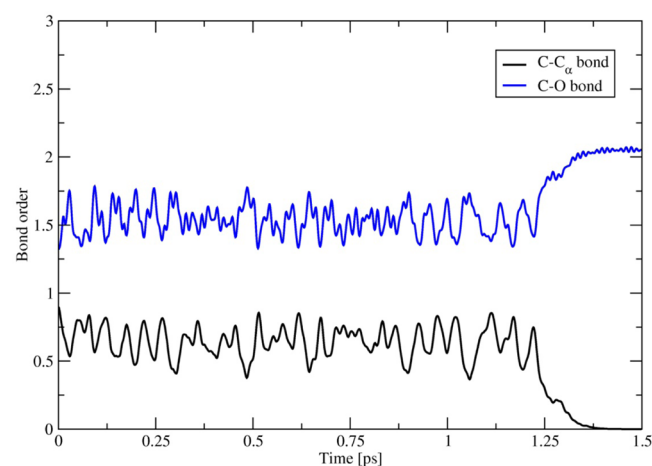


Figure 7. Bond orders of the C–C<sub>α</sub> bond and the C–O bond versus time.

The C–C<sub>α</sub> bond is cleaved at about 1338 fs (cutoff distance of 2.5 Å was reached). This can be also seen from this graph: The bond order of C–C<sub>α</sub> changes from approximately 1 to 0. Note that the drop to half bond order occurs prior to reaching 1338 fs (at about 1231 fs). The bond order reaches 0 at about 1393 fs. The definition of the cleavage point can therefore

be newly defined according to the change in bond order. At the same time, the C–O bond order changes from 1.5 to approximately 2. Initially the bond order of this bond (carbonyl group) is 1.5 due to the triplet state. The triplet state involves an excitation of an electron from a nonbonding orbital located on the C=O double bond to a  $\pi^*$  orbital located in the same area. Initially the overall bond order on the C atom is 3.7 (C–O bond order = 1.3, C–H bond order = 0.8, C–C<sub>α</sub> bond order = 0.9, the electron of the excitation is not involved in bonding and is located on the C atom = 0.5, and the sum is 3.7). The overall bond order at C changes from 3.7 to 3.2 after the cleavage. The fragment consists of C doubly bonded to O and singly bonded (bond order of 0.7) to H. The nonbonded electron is still located on C. The total bond order change on C can be explained by a homolytic cleavage of the C–C<sub>α</sub> bond. The main change during the cleavage is the transfer of one electron from the C–C<sub>α</sub> bond to the C=O bond (bond order there increases from 1.5 to 2). The C<sub>α</sub> atom (on the other fragment) remains a total bond order of about 3.8.

Another insight into this reaction comes from the Mulliken charge analysis on the trajectory; see Figure 8.

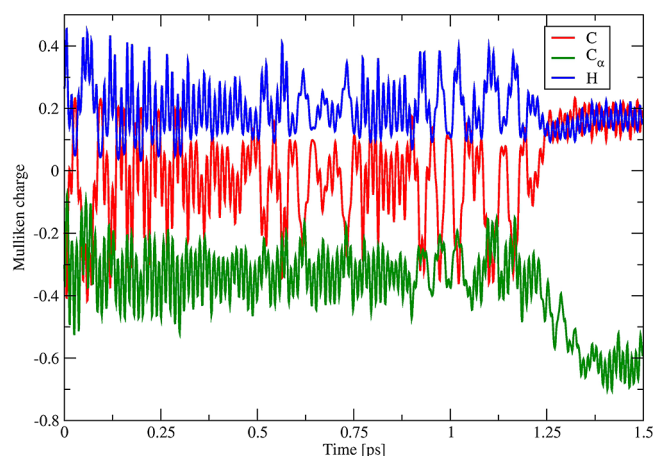
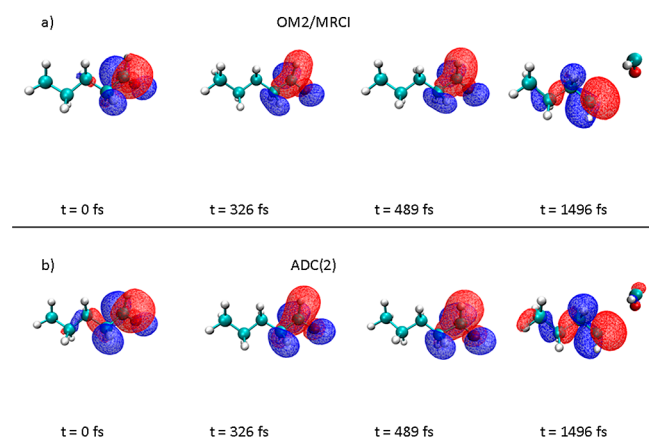


Figure 8. Mulliken charges along the trajectory.

Most of the charges remain relatively constant with oscillations due to vibrational motion. Main changes can be seen in C, C<sub>α</sub> and H. The charge of O remains at a constant value of –0.3 au. By adding the charges of C and H, this yields an almost zero charge on the CHO fragment after cleavage. This is consistent with the bond order analysis. Both properties predict a homolytic bond cleavage.

The HOMO orbital itself is very important since it is involved in different excitations. Figure 9 shows the HOMO orbital during one sample trajectory of C–C<sub>α</sub> bond cleavage. The HOMO orbital is calculated on-the-fly by OM2/MRCI and, as validation, also with ADC(2) on corresponding C–C<sub>α</sub> distances. From the figure, it can be seen that there are only slight changes in the first 500 fs in the orbital. These changes are also recovered by the ADC(2) method. The HOMO orbital can be described as a  $\pi^*$  orbital. After the cleavage, the HOMO orbital now resides on the larger fragment. ADC(2) predicts a very similar orbital. Such good agreement between the HOMO orbitals calculated by OM2/MRCI and ADC(2) emphasizes again the similarity of different properties calculated by OM2/MRCI and ADC(2). This validates the usage of the semiempirical methods for this particular reaction.





**Figure 9.** HOMO orbital structure for snapshots in the dynamics of C–C $_{\alpha}$  cleavage (a) as calculated by OM2/MRCI and (b) as calculated by ADC(2).

The following summary from the insight gained here about the Norrish type I reaction is provided: Norrish type I reaction is the dominant process in the short time scale regime, although the overall yield is very low (about 7–9% depending on the temperature). The reaction is taking place on the lowest triplet state. The time scale of the reaction is in the picosecond range and takes place before extensive energy redistribution is possible.

**3.6. Mechanistic Insight into the Norrish Type II Reaction: Energetics, Bond Orders, and Mulliken Charges.** One trajectory run adiabatically on the lowest triplet state surface at 200 K shows the first step of the Norrish type II reaction, namely, the  $\gamma$ -H transfer to the C=O group.

Figure 10 shows snapshots of this reaction.

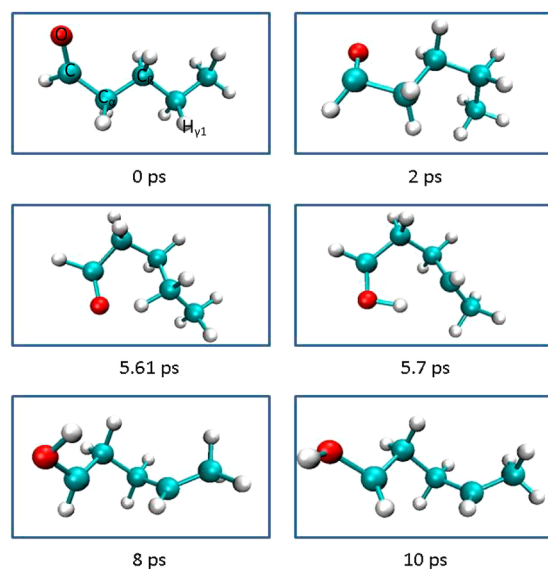


**Figure 10.** Snapshots of the  $\gamma$ -H transfer.

The snapshots show various configurations along the dynamics. Initially the  $\gamma$ -H is far away from the carbonyl group. The system has to reach the right configuration for the  $\gamma$ -H transfer. Therefore, the time scale of this process is much longer than for the simple C–C $_{\alpha}$  cleavage. Because of this, most of the trajectories reach first the cleavage of the C–C $_{\alpha}$

bond. In the gas phase, both fragments separate from each other. For condensed phases, it might be possible that the fragments recombine and then further react through the Norrish type II reaction. Additionally, the solvent itself might help to transfer the  $\gamma$ -H atom (for example, through a hydrogen bond bridge in water). It is therefore expected that in condensed phases the yields for Norrish II reaction is higher than for Norrish type I. Additional simulations of pentanal in condensed phase are planned to verify the prediction of the different yields.

Figure 11a shows temporal change of the potential energy surface along this trajectory. For clarity, the lower part of

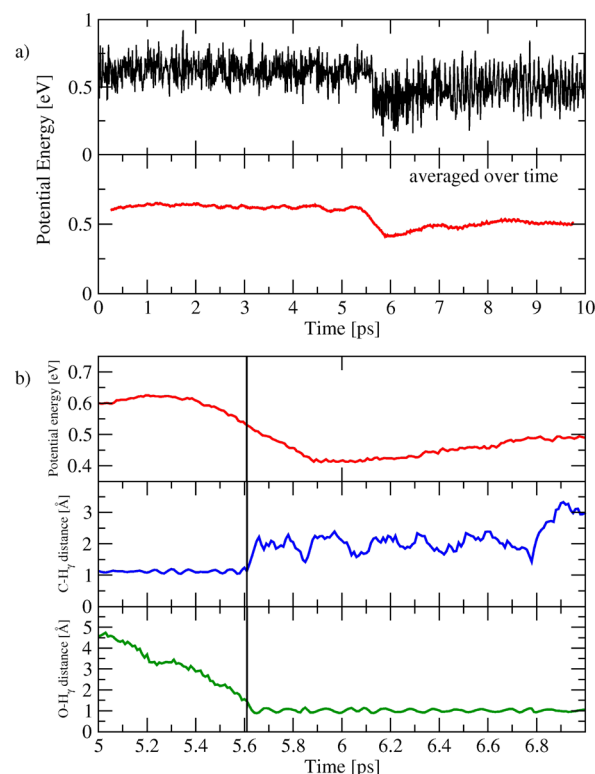


**Figure 11.** (a) Temporal change in the potential energy along the trajectory and the lower part smoothed over time. (b) Enlargement of potential energy surface between 5 and 7 ps and C–H $_{\gamma}$  and O–H $_{\gamma}$  distances in this time scale.

Figure 11a shows the smoothed potential energy. The reference energy of these graphs is the pentanal minimum energy. Figure 11b shows an enlargement of the smoothed potential energy in the region between 5 and 7 ps, the time scale where the  $\gamma$ -H transfer occurs. Additionally, important bond lengths (C–H $_{\gamma}$  distance and O–H $_{\gamma}$  distance) that change during the  $\gamma$ -H transfer are also shown. Energetically, the total energy of the triplet transition state (structure at 5.61 ps) is about 0.59 eV higher than triplet minimum structure and about 3.52 eV higher than the singlet minimum structure. Comparing the initial excitation energy to the first excited state (3.76 eV), this barrier can be easily overcome. The optimization of the transition state was unsuccessful. Optimization might lead to a lower energy difference. The same transition state was estimated in heptanal<sup>15</sup> about 0.3 eV higher than the minimum. After H transfer, the potential energy is lower than before, suggesting a larger stabilization of the newly created structure compared to the initial isomer.

Figure 12 shows a minimized energy path between the minimum of pentanal and the structure after H transfer. It was

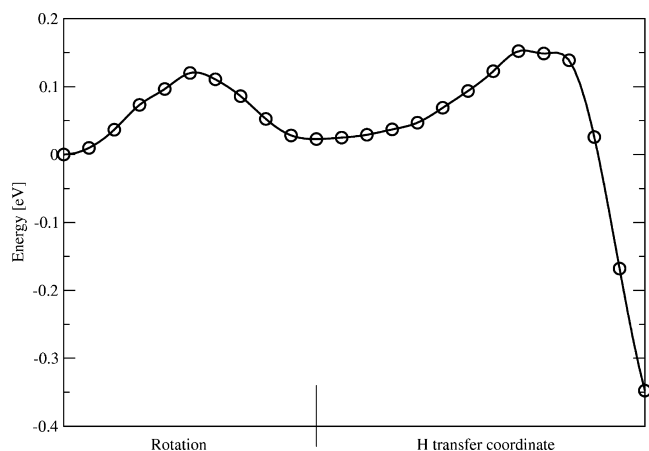


**Figure 12.** Potential energy surface along a minimum energy path between initial structure and final structure after H transfer. It is assumed that first a rotation about the  $C_\alpha$ – $C_\beta$  bond takes place and then the  $\gamma$ -H is transferred.

assumed that first the system performs a rotation along the  $C_\alpha$ – $C_\beta$  bond to achieve proximity between the H-donor and the H-acceptor group, and then in a second step, the hydrogen is transferred. This figure has been created by using one constraint for each part (dihedral angle and H–O distance, respectively) and is therefore one possible minimum energy path. As can be seen from this figure, the rotational barrier is about 0.12 eV high; the barrier for the H transfer is about 0.15 eV high. Energetically the barrier is therefore much lower than the barrier for the C– $C_\alpha$  cleavage. Also here, as seen previously in Figure 11, the energy of the newly created structure after H transfer is more stabilized by about 0.35 eV than the energy of the minimum energy structure of pentanal.

Also here, this trajectory was further analyzed using properties such as bond orders and Mulliken charges.

Figure 13 shows the bond order along this trajectory: C is connected to O,  $C_\alpha$  and H. Since the trajectory starts on a

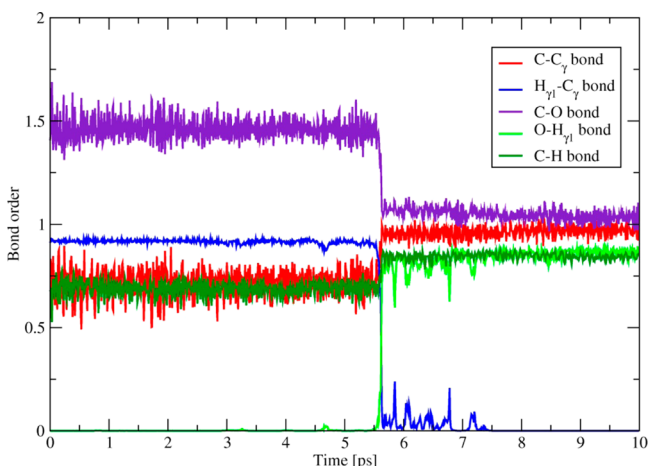


**Figure 13.** Bond order changes along the  $\gamma$ -H transfer to the C=O group.

triplet surface, two electrons are initially unpaired with the same spin. The total bond order (sum over all bond orders along

bonds and bond order of unbounded electrons) on atom C is about 3.5–3.7 during the dynamics. The initial bond order of the C–O bond is 1.5 (not 2 as on the singlet surface). The bond order of the other bond connected to C (atoms H and  $C_\alpha$ ) is 0.75 (not 1 as on the singlet surface). Comparing all the bond orders along all bonds to the total value yields a difference of 0.5 in bond order. This corresponds to an unpaired electron on the C atom, a radical. The triplet state is a biradical state, and the second unpaired electron is between C and O (therefore, a bond order of 1.5). The H atom that is transferred ( $H_{\gamma 1}$ ) is initially connected to  $C_\gamma$ , bond order 1. At the point of the transfer, the bond order changes to 0 (i.e., the bond is cleaved), and instead, a bond order of 1 is created between  $H_{\gamma 1}$  and O. The bond order between C and O changes to 1, the bond orders of H–C and C– $C_\alpha$  change from 0.75 to 0.5. This means that two electrons around the C were used for creating the new O– $H_{\gamma 1}$  bond. Looking at the total bond order of  $C_\gamma$  reveals that this value stays constant at about 4, although the total bonds change from 4 to 3. This means that the two electrons that were used for the bond between  $C_\gamma$  and  $H_{\gamma 1}$  do not move from the  $C_\gamma$ . The H is therefore transferred without its electron; correctly it is therefore an  $H^+$  transfer.

Figure 14 shows the Mulliken charges along this trajectory.

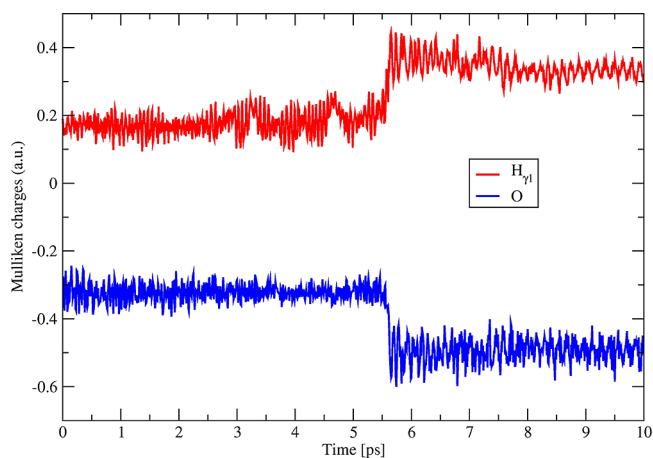


**Figure 14.** Mulliken charge along the trajectory.

Charges of other atoms mainly remain constant along the trajectory. Averaged values are summarized in Table 6.

**Table 6.** Average Mulliken Charge of All Atoms

atom	average Mulliken charge (a.u.)
all hydrogens except $H_{\gamma 1}$	0.2
$C_\alpha$ , $C_\beta$ , $C_\gamma$	−0.3
$C_\delta$	−0.6
C	−0.1

Most of the Mulliken charges do not change much during the dynamics. The O becomes much more negative, and the  $H_{\gamma 1}$  becomes much more positive following transfer to O, as seen in the graph.

**3.7. H Detachment Mechanism in Pentanal.** One trajectory run adiabatically on the lowest triplet state surface at 300 K shows H detachment. This H detachment has been

described as a minor fragmentation pathway for aldehydes.<sup>7,26</sup> Figure 15 shows snapshots from this trajectory.

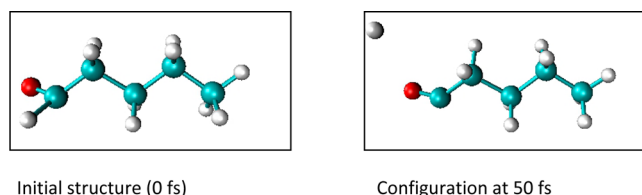


**Figure 15.** H detachment of pentanal.

A cutoff distance of 2.5 Å was defined. This distance was reached after 25.5 fs. Bond order and Mulliken charges confirm that an H atom is detached from the molecule. Estimates for H detachment in heptanal<sup>15</sup> ranges from 6.9 kcal/mol (detachment of  $\gamma$ -H), 7.7 kcal/mol (detachment of  $\delta$ -H), and 10.4 kcal/mol (detachment of  $\epsilon$ -H), up to 17.8 kcal/mol (detachment of  $\beta$ -H). The barrier for H detachment seen here has not been calculated. However, this barrier was estimated to lie in the range of 6.9 to 17.8 kcal/mol. In ref 26, the barrier high for this specific H detachment in butanal has been estimated to be 17.7 kcal/mol. Therefore, the barrier here in pentanal is estimated to be closer to the high limit of the H detachment barrier range given above, around 17.7 kcal/mol. For comparison, the barrier for C–C $_{\alpha}$  cleavage has been estimated in the same work of heptanal to be 11.3 kcal/mol. The energy for the C–C $_{\alpha}$  cleavage is therefore lower than the H detachment barrier. It can therefore be assumed that these reaction channels are competitive. However, in this study, the yield for the H detachment is lower than the yield of Norrish type I reaction. It is assumed that this can be explained by the higher barrier for detachment, as also argued in ref 26.

No trajectory has been observed that shows the roaming behavior seen in small aldehydes. This pathway might be inaccessible for large aldehydes or happen only very rarely.

**3.8. Effect of Long Time Scale Simulation on Norrish I/II Ratio.** Section 3.3. summarizes the statistics of various reactions observed at short and long time scales. It has been observed that for longer time scales (up to 100 ps) the theoretically predicted relative yields of the Norrish I and Norrish II reactions (34% vs 66%, respectively) now approach the experimental relative yields of 80% for the Norrish type II reaction.<sup>25,28</sup> Figure 16 shows a histogram of the time scale of Norrish type I/II reactions.

As can be seen from this figure, the Norrish type I reaction happens on two time scales: one is ultrafast and below 10 ps, and the second one is slower, starting at 45 ps. On the contrary, the Norrish type II reaction only starts after 20 ps. This explains why the short time scale simulations only provided one trajectory for this reaction path. The following interpretation is suggested for the time scale and the statistics of Norrish I vs Norrish II reactions.

Looking at structural changes, it seems reasonable to assume that Norrish type I reaction should be favored since the first step involves only a cleavage of a bond, whereas the Norrish type II reaction involves also large structural rearrangement before an H atom is transferred. Additionally, considering dissociation energies, the C–C dissociation energy is also lower than the C–H energy. However, the Norrish type II cleavage happens simultaneously with the creation of a new O–H bond, so that the total energy needed for the reaction is lower compared to

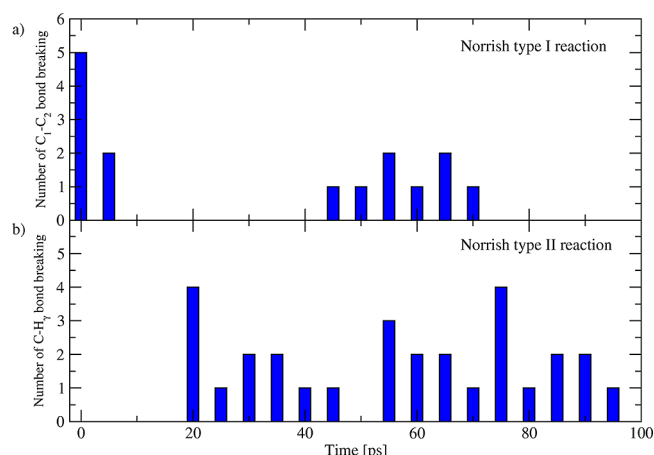


**Figure 16.** Histogram of (a) Norrish type I reactions and (b) Norrish type II reactions in the time scale of 100 ps.

Norrish type I reaction. This is also expressed in the  $\Delta H$  calculated in ref 28: a value of 348.3 kJ/mol is predicted for the Norrish type I reaction, compared with 82.2 kJ/mol for the Norrish type II reaction. In summary, considering the structure only, Norrish type I reaction is favored, and including energetic aspects, Norrish type II reaction is preferred. This is also seen in the simulations: Norrish type II reactions occur on a longer time scale compared to Norrish type I, but with a higher yield.

Another important effect on the Norrish I/II ratio is the occurrence of intramolecular vibrational energy redistribution. Statistical theories such as RRKM assume a time scale of about 10 ps for efficient IVR. The Norrish type I reaction therefore occurs before full IVR has taken place, whereas for the Norrish type II reaction the opposite is true (time scales longer than 20 ps). More specifically, these findings here show that the  $\gamma$ -H transfer sets in at larger times, hinting that IVR is essential for the Norrish type II reaction. The longer the carbon chain (the larger the system), the more IVR is expected. Thus, for larger aldehydes, more Norrish type II can be expected.

Different factors might affect the discrepancy between the theoretical and experimental yields for Norrish I/II reactions. One possible factor is the occurrence of collisions in experiments. So all the experiments, also those in gas phase, were done in conditions where collisions are possible. The existence of collisions in the gas phase in sufficient pressure is therefore expected. The experimental studies are therefore not in an isolated system. The role of the collisions can be very large, as in RRKM theory. It is not claimed that this provides a complete understanding of the experimental outcome of the yields of Norrish I vs Norrish II, but these calculations do give a lot of insight into the mechanistic aspects of Norrish I and Norrish II. Besides collision, there could be also other factors (such as whether O<sub>2</sub> or N<sub>2</sub> is used; see ref 28), which affect the yield of Norrish I and II.

#### 4. CONCLUSIONS

Photoexcitation dynamics of pentanal has been simulated theoretically using dynamics on the semiempirical OM2 potential. Additional calculations on the singlet and triplet excited state were performed using the nonadiabatic surface hopping method with the OM2/MRCI potential. The OM2 potential energy surface reproduces important stationary points correctly. Quantitatively the energetics obtained by OM2/MRCI are in good agreement with the ab initio method ADC(2) and with



the experiment. It is concluded that the OM2/MRCI potential is a very reliable potential. The advantage of this method is the large reduction in computational cost for this system. The usage of this potential is recommended for large systems especially in dynamical simulations.

From the simulations, it is concluded that the reactions are not taking place on the singlet surface (at least not in the time scale that was simulated). However, one triplet state is very close to the excited singlet state, and intersystem crossing between these states is assumed to take place. The reactions are found to take place on the lowest triplet potential surface. The system does not switch to a different triplet state, in the course of the dynamics. These results establish that additional triplet states can be neglected in the treatment of photochemical reactions.

Properties such as bond orders and Mulliken charges are used to further analyze the first step in the Norrish type I reaction. Both properties show that the C–C $\alpha$  bond cleavage is homolytic and that two radical fragments are produced.

In the short time scale of up to 10 ps in one trajectory, the first step of the Norrish type II reaction was seen, namely, the  $\gamma$ -H transfer. The time scale of this process is about 5 ps. No evidence for triplet transitions in the Norrish type II reaction has been observed. Analysis using Mulliken charges and bond orders reveals that an H $^+$  is transferred from the C $\gamma$  to the carbonyl oxygen. The time scale for this process is longer than for the C–C $\alpha$  cleavage. The reason for this is that the system has first to find the right configuration for the H $^+$  transfer, and this takes time.

Another trajectory shows the H detachment. The time scale for this process is ultrafast, shorter than 1 ps.

Only about 10% of the trajectories were reactive in the time scale of 10 ps. This implies that the time scale for reactions is usually longer than 10 ps.

In the short time scale of up to 10 ps, Norrish type I reaction is clearly preferred over reactions involving H detachment ( $\gamma$ -H transfer in Norrish type II reaction and H detachment at the carbonyl carbon). It is suggested that in condensed phase the situation is different. Hydrogen networks in condensed phase might assist the H transfer, such that the yield for Norrish type II reaction is much higher than Norrish type I reaction.

The ratio between Norrish type I and II reactions is different, if long time scales up to 100 ps are considered. More Norrish type II reactions have been observed in the long time scale, all of them are happening after at least 20 ps. The statistics now show in 27% of the trajectories Norrish type II reactions, 14% Norrish type I reactions, and 1% H detachment. The opening of Norrish type II reaction was explained by considering the following factors: from a structural point of view, the  $\gamma$ -H transfer can be only performed, if a critical configuration of near vicinity of the  $\gamma$ -H and carbonyl oxygen is reached. From an energetic point of view, the  $\gamma$ -H transfer seems to happen only after IVR has taken place. Both factors imply a larger time scale for the Norrish type II process than the simple C–C $\alpha$  cleavage in Norrish type I.

Additionally, from the energetic point of view, it has been shown, that the barrier for the Norrish type II reaction is substantially smaller than for the Norrish type I reaction. Thus, the following factors favor the Norrish type II reaction for larger aldehydes: lower energy barrier compared to Norrish type I reaction and faster IVR (due to larger numbers of degrees of freedom). In summary, Norrish I is essentially direct, while Norrish II should benefit from a geometric change

(that requires also energy redistribution in the molecule, taking more than 10 ps). The results are also very suggestive with regard to the effect of collisions in gas phase or with regard to the corresponding processes in solution: the collisions (or condensed phase) will give preference to Norrish II over Norrish I since these conditions favor more statistical, less direct, dynamics.

In summary, dynamics using a semiempirical potential for the simulation of the photoexcitation of pentanal has been applied. The reduced computational cost makes this methodology applicable to a wide range of photoexcitation processes of large organic systems. A natural continuation of this study is the investigation of the photoexcitation of pentanal in an environment and the photoexcitation of larger aldehydes. For pentanal, the simulation predicts that the Norrish type I reaction is favored. It would be interesting to study larger aldehydes and to explore from which aldehyde length the Norrish type II reaction is dominant.

## AUTHOR INFORMATION

### Corresponding Author

\*Tel: +972-26585732. Fax: +972-2-6513742. E-mail: doritsh@fh.huji.ac.il (D.S.); benny@fh.huji.ac.il (R.B.G.); lanzg@qibebt.ac.cn (Z.L.).

### Notes

The authors declare no competing financial interest.

## ACKNOWLEDGMENTS

We thank Prof. S. A. Nizkorodov for the introduction into the photochemistry of aldehydes. We acknowledge Prof. W. Thiel for helpful insight into the MNDO package. D.S. acknowledges a Lady Davis Fellowship at the HU. This research was supported by the Israel Science Foundation, Grant No. 172/12, and by NSF (USA) through EMSI at UC Irvine (Grants 0431312 and 0909227). Z.L. thanks the partial supports from the CAS 100 Talent Project, NSFC project (Grant Nos. 21103213 and 91233106), and the Director Innovation Foundation of CAS-QIBEBT. Additionally, Z.L. appreciates the Super Computing Center, Computer Network Information Center, CAS, for support.

## REFERENCES

- (1) Atkinson, R. Gas-Phase Tropospheric Chemistry of Organic Compounds: a Review. *Atmos. Environ., Part A* **1990**, *24*, 1–41.
- (2) Graedel, T. E.; Farrow, L. A.; Weber, T. A. Kinetic Studies of Photochemistry of Urban Troposphere. *Atmos. Environ.* **1976**, *10*, 1095–1116.
- (3) Grosjean, D. Formaldehyde and Other Carbonyls in Los-Angeles Ambient Air. *Environ. Sci. Technol.* **1982**, *16*, 254–262.
- (4) Finlayson-Pitts, B. J.; Pitts, J. N. *Atmospheric Chemistry*; John Wiley: New York, 1986.
- (5) Calvert, J. G.; Pitts, J. N. *Photochemistry*; John Wiley: New York, 1966.
- (6) Lee, E. K. C.; Lewis, R. S. Photochemistry of Simple Aldehydes and Ketones in the Gas Phase. *Adv. Photochem.* **1980**, *12*, 1–96.
- (7) Kurosaki, Y. Hydrogen-Atom Production Channels of Acetaldehyde Photodissociation: Direct DFT Molecular Dynamics Study. *J. Mol. Struct.* **2008**, *850*, 9–16.
- (8) Amaral, G. A.; Arregui, A.; Rubio-Lago, L.; Rodriguez, J. D.; Banares, L. Imaging the Radical Channel in Acetaldehyde Photodissociation: Competing Mechanisms at Energies Close to the Triplet Exit Barrier. *J. Chem. Phys.* **2010**, *133*, 064303.
- (9) Fu, B. N.; Shepler, B. C.; Bowman, J. M. Three-State Trajectory Surface Hopping Studies of the Photodissociation Dynamics of

Formaldehyde on ab Initio Potential Energy Surfaces. *J. Am. Chem. Soc.* **2011**, *133*, 7957–7968.

(10) Fang, W. H. Ab initio Determination of Dark Structures in Radiationless Transitions for Aromatic Carbonyl Compounds. *Acc. Chem. Res.* **2008**, *41*, 452–457.

(11) Townsend, D.; Lahankar, S. A.; Lee, S. K.; Chambreau, S. D.; Suits, A. G.; Zhang, X.; Rheinecker, J.; Harding, L. B.; Bowman, J. M. The Roaming Atom: Straying from the Reaction Path in Formaldehyde Decomposition. *Science* **2004**, *306*, 1158–1161.

(12) Ashfold, M. N. R.; Glowacki, D. R. Photochemistry: Scrambled by the Sun? *Nat. Chem.* **2011**, *3*, 423–424.

(13) Heazlewood, B. R.; Maccarone, A. T.; Andrews, D. U.; Osborn, D. L.; Harding, L. B.; Klippenstein, S. J.; Jordan, M. J. T.; Kable, S. H. Near-Threshold H/D Exchange in CD(3)CHO Photodissociation. *Nat. Chem.* **2011**, *3*, 443–448.

(14) Tadic, J. M.; Moortgat, G. K.; Bera, P. P.; Loewenstein, M.; Yates, E. L.; Lee, T. J. Photochemistry and Photophysics of *n*-Butanal, 3-Methylbutanal, and 3,3-Dimethylbutanal: Experimental and Theoretical Study. *J. Phys. Chem. A* **2012**, *116*, 5830–5839.

(15) Paulson, S. E.; Liu, D. L.; Orzechowska, G. E.; Campos, L. M.; Houk, K. N. Photolysis of Heptanal. *J. Org. Chem.* **2006**, *71*, 6403–6408.

(16) Tadic, J. M.; Xu, L.; Houk, K. N.; Moortgat, G. K. Photooxidation of *n*-Octanal in Air: Experimental and Theoretical Study. *J. Org. Chem.* **2011**, *76*, 1614–1620.

(17) Thompson, K. C.; Crittenden, D. L.; Kable, S. H.; Jordan, M. J. T. A Classical Trajectory Study of the Photodissociation of T-1 Acetaldehyde: The Transition from Impulsive to Statistical Dynamics. *J. Chem. Phys.* **2006**, *124*, 044302.

(18) Han, Y. C.; Shepler, B. C.; Bowman, J. M. Quasiclassical Trajectory Calculations of the Dissociation Dynamics of CH(3)CHO at High Energy Yield Many Products. *J. Phys. Chem. Lett.* **2011**, *2*, 1715–1719.

(19) Cordeiro, M. N. D. S.; Martinez-Nunez, E.; Fernandez-Ramos, A.; Vazquez, S. A. Direct Dynamics Study of the Photodissociation of Triplet Propanal at Threshold. *Chem. Phys. Lett.* **2003**, *381*, 37–44.

(20) Metha, G. F.; Terentis, A. C.; Kable, S. H. Near Threshold Photochemistry of Propanal. Barrier Height, Transition State Structure, and Product State Distributions for the HCO Channel. *J. Phys. Chem. A* **2002**, *106*, 5817–5827.

(21) Kurosaki, Y. Energy-Flow Dynamics in the Molecular Channel of Propanal Photodissociation,  $C_2H_5CHO \rightarrow C_2H_6 + CO$ : Direct ab Initio Molecular Dynamics Study. *J. Phys. Chem. A* **2006**, *110*, 11230–11236.

(22) Buntine, M. A.; Lee, C.; Metha, G. F. The Lowest-Lying Excited Singlet and Triplet Electronic States of Propanal: an ab Initio Molecular Orbital Investigation of the Potential Energy Surfaces. *Phys. Chem. Chem. Phys.* **2004**, *6*, 688–696.

(23) Dewar, M. J. S.; Doubleday, C. MINDO-3 Study of Norrish Type-II Reaction of Butanal. *J. Am. Chem. Soc.* **1978**, *100*, 4935–4941.

(24) Sauters, R. R.; Edberg, L. A. Modeling of Norrish Type-II Reactions by Semiempirical and ab-Initio Methodology. *J. Org. Chem.* **1994**, *59*, 7061–7066.

(25) Tadic, J.; Juranic, I.; Moortgat, G. K. Pressure Dependence of the Photooxidation of Selected Carbonyl Compounds in Air: *n*-butanal and *n*-pentanal. *J. Photochem. Photobiol., A* **2001**, *143*, 169–179.

(26) Chen, X. B.; Fang, W. H. Norrish I vs II Reactions of Butanal: a Combined CASSCF, DFT and MP2 Study. *Chem. Phys. Lett.* **2002**, *361*, 473–482.

(27) Zhu, L.; Cronin, T.; Narang, A. Wavelength-Dependent Photolysis of *i*-Pentanal and *t*-Pentanal from 280 to 330 nm. *J. Phys. Chem. A* **1999**, *103*, 7248–7253.

(28) Cronin, T. J.; Zhu, L. Dye Laser Photolysis of *n*-Pentanal from 280 to 330 nm. *J. Phys. Chem. A* **1998**, *102*, 10274–10279.

(29) Zhu, L.; Tang, Y. X.; Chen, Y. Q.; Cronin, T. Wavelength-Dependent Photolysis of C3–C7 Aldehydes in the 280–330 nm Region. *Spectrosc. Lett.* **2009**, *42*, 467–478.

(30) Tadic, J.; Juranic, I.; Moortgat, G. K. Photooxidation of *n*-Hexanal in Air. *Molecules* **2001**, *6*, 287–299.

(31) Tang, Y. X.; Zhu, L. Wavelength-Dependent Photolysis of *n*-Hexanal and *n*-Heptanal in the 280–330-nm Region. *J. Phys. Chem. A* **2004**, *108*, 8307–8316.

(32) Tadic, J. M.; Juranic, I. O.; Moortgat, G. K. Photooxidation of *n*-Heptanal in Air: Norrish Type I and II Processes and Quantum Yield Total Pressure Dependency. *J. Chem. Soc., Perkin Trans. 2* **2002**, 135–140.

(33) Shemesh, D.; Gerber, R. B. Classical Trajectory Simulations of Photoionization Dynamics of Tryptophan: Intramolecular Energy Flow, Hydrogen-Transfer Processes and Conformational Transitions. *J. Phys. Chem. A* **2006**, *110*, 8401–8408.

(34) Shemesh, D.; Gerber, R. B. Different Chemical Dynamics for Different Conformers of Biological Molecules: Photoionization of Glycine. *J. Chem. Phys.* **2005**, *122*, 241104.

(35) Shemesh, D.; Baer, R.; Seideman, T.; Gerber, R. B. Photoionization Dynamics of Glycine Adsorbed on a Silicon Cluster: "On-the-Fly" Simulations. *J. Chem. Phys.* **2005**, *122*, 184704.

(36) Shemesh, D.; Chaban, G. M.; Gerber, R. B. Photoionization Dynamics of Glycine: The First 10 ps. *J. Phys. Chem. A* **2004**, *108*, 11477–11484.

(37) Miller, Y.; Chaban, G. M.; Finlayson-Pitts, B. J.; Gerber, R. B. Photochemical Processes Induced by Vibrational Overtone Excitations: Dynamics Simulations for *cis*-HONO, *trans*-HONO, HNO<sub>3</sub>, and HNO<sub>3</sub>–H<sub>2</sub>O. *J. Phys. Chem. A* **2006**, *110*, 5342–5354.

(38) Miller, Y.; Gerber, R. B. Dynamics of Vibrational Overtone Excitations of H<sub>2</sub>SO<sub>4</sub>, H<sub>2</sub>SO<sub>4</sub>–H<sub>2</sub>O: Hydrogen-Hopping and Photodissociation Processes. *J. Am. Chem. Soc.* **2006**, *128*, 9594–9595.

(39) Shmilovits-Ofir, M.; Miller, Y.; Gerber, R. B. Conformational Transitions of Glycine Induced by Vibrational Excitation of the O–H Stretch. *Phys. Chem. Chem. Phys.* **2011**, *13*, 8715–8722.

(40) Shmilovits-Ofir, M.; Gerber, R. B. Proton Transfer and Dissociation of GlyLysH<sup>+</sup> following O–H and N–H Stretching Mode Excitations: Dynamics Simulations. *J. Am. Chem. Soc.* **2011**, *133*, 16510–16517.

(41) Wu, X.; Koslowski, A.; Thiel, W. Semiempirical Quantum Chemical Calculations Accelerated on a Hybrid Multicore CPU-GPU Computing Platform. *J. Chem. Theory Comput.* **2012**, *8*, 2272–2281.

(42) Korth, M.; Thiel, W. Benchmarking Semiempirical Methods for Thermochemistry, Kinetics, and Noncovalent Interactions: OMx Methods Are Almost As Accurate and Robust As DFT-GGA Methods for Organic Molecules. *J. Chem. Theory Comput.* **2011**, *7*, 2929–2936.

(43) Fabiano, E.; Thiel, W. Nonradiative Deexcitation Dynamics of 9H-Adenine: An OM2 Surface Hopping Study. *J. Phys. Chem. A* **2008**, *112*, 6859–6863.

(44) Lan, Z. G.; Fabiano, E.; Thiel, W. Photoinduced Nonadiabatic Dynamics of Pyrimidine Nucleobases: On-the-Fly Surface-Hopping Study with Semiempirical Methods. *J. Phys. Chem. B* **2009**, *113*, 3548–3555.

(45) Lan, Z. G.; Fabiano, E.; Thiel, W. Photoinduced Nonadiabatic Dynamics of 9H-Guanine. *ChemPhysChem* **2009**, *10*, 1225–1229.

(46) Lu, Y.; Lan, Z. G.; Thiel, W. Hydrogen Bonding Regulates the Monomeric Nonradiative Decay of Adenine in DNA Strands. *Angew. Chem., Int. Ed.* **2011**, *50*, 6864–6867.

(47) Kazaryan, A.; Lan, Z. G.; Schafer, L. V.; Filatov, M.; Thiel, W. Surface Hopping Excited-State Dynamics Study of the Photoisomerization of a Light-Driven Fluorene Molecular Rotary Motor. *J. Chem. Theory Comput.* **2011**, *7*, 2189–2199.

(48) Weingart, O.; Lan, Z. G.; Koslowski, A.; Thiel, W. Chiral Pathways and Periodic Decay in *cis*-Azobenzene Photodynamics. *J. Phys. Chem. Lett.* **2011**, *2*, 1506–1509.

(49) Lan, Z. G.; Lu, Y.; Fabiano, E.; Thiel, W. QM/MM Nonadiabatic Decay Dynamics of 9H-Adenine in Aqueous Solution. *ChemPhysChem* **2011**, *12*, 1989–1998.

(50) Strodel, P.; Tavan, P. A Revised MRCI-Algorithm Coupled to an Effective Valence-Shell Hamiltonian. II. Application to the Valence Excitations of Butadiene. *J. Chem. Phys.* **2002**, *117*, 4677–4683.

(51) Wanko, M.; Hoffmann, M.; Strodel, P.; Koslowski, A.; Thiel, W.; Neese, F.; Frauenheim, T.; Elstner, M. Calculating Absorption Shifts

for Retinal Proteins: Computational Challenges. *J. Phys. Chem. B* **2005**, *109*, 3606–3615.

(52) Hoffmann, M.; Wanko, M.; Strodel, P.; König, P. H.; Frauenheim, T.; Schulten, K.; Thiel, W.; Tajkhorshid, E.; Elstner, M. Color Tuning in Rhodopsins: The Mechanism for the Spectral Shift between Bacteriorhodopsin and Sensory Rhodopsin II. *J. Am. Chem. Soc.* **2006**, *128*, 10808–10818.

(53) Silva-Junior, M. R.; Thiel, W. Benchmark of Electronically Excited States for Semiempirical Methods: MNDO, AM1, PM3, OM1, OM2, OM3, INDO/S, and INDO/S2. *J. Chem. Theory Comput.* **2010**, *6*, 1546–1564.

(54) Silva-Junior, M. R.; Schreiber, M.; Sauer, S. P. A.; Thiel, W. Benchmarks of Electronically Excited States: Basis Set Effects on CASPT2 Results. *J. Chem. Phys.* **2010**, *133*, 174318.

(55) Shemesh, D.; Gerber, R. B. Femtosecond Timescale Deactivation of Electronically Excited Peroxides at Ice Surfaces. *Mol. Phys.* **2012**, *110*, 605–617.

(56) Epstein, S. A.; Shemesh, D.; Tran, V. T.; Nizkorodov, S. A.; Gerber, R. B. Absorption Spectra and Photolysis of Methyl Peroxide in Liquid and Frozen Water. *J. Phys. Chem. A* **2012**, *116*, 6068–6077.

(57) Weber, W.; Thiel, W. Orthogonalization Corrections for Semiempirical Methods. *Theor. Chem. Acc.* **2000**, *103*, 495–506.

(58) Kosłowski, A.; Beck, M. E.; Thiel, W. Implementation of a General Multireference Configuration Interaction Procedure with Analytic Gradients in a Semiempirical Context using the Graphical Unitary Group Approach. *J. Comput. Chem.* **2003**, *24*, 714–726.

(59) Weigend, F.; Haser, M. RI-MP2: First Derivatives and Global Consistency. *Theor. Chem. Acc.* **1997**, *97*, 331–340.

(60) Ahlrichs, R.; Bar, M.; Haser, M.; Horn, H.; Kolmel, C. Electronic–Structure Calculations on Workstation Computers: the Program System Turbomole. *Chem. Phys. Lett.* **1989**, *162*, 165–169.

(61) Schirmer, J. Beyond the Random-Phase Approximation: a New Approximation Scheme for the Polarization Propagator. *Phys. Rev. A* **1982**, *26*, 2395–2416.

(62) Dunning, T. H. Gaussian-Basis Sets for Use in Correlated Molecular Calculations 0.1. The Atoms Boron through Neon and Hydrogen. *J. Chem. Phys.* **1989**, *90*, 1007–1023.

(63) Sobolewski, A. L.; Shemesh, D.; Domcke, W. Computational Studies of the Photophysics of Neutral and Zwitterionic Amino Acids in an Aqueous Environment: Tyrosine–(H<sub>2</sub>O)<sub>2</sub> and Tryptophan–(H<sub>2</sub>O)<sub>2</sub> Clusters. *J. Phys. Chem. A* **2009**, *113*, 542–550.

(64) Shemesh, D.; Sobolewski, A. L.; Domcke, W. Role of Excited-State Hydrogen Detachment and Hydrogen-Transfer Processes for the Excited-State Deactivation of an Aromatic Dipeptide: N-Acetyl Tryptophan Methyl Amide. *Phys. Chem. Chem. Phys.* **2010**, *12*, 4899–4905.

(65) Shemesh, D.; Hattig, C.; Domcke, W. Photophysics of the Trp–Gly Dipeptide: Role of Electron and Proton Transfer Processes for Efficient Excited-State Deactivation. *Chem. Phys. Lett.* **2009**, *482*, 38–43.

(66) Shemesh, D.; Sobolewski, A. L.; Domcke, W. Efficient Excited-State Deactivation of the Gly–Phe–Ala Tripeptide via an Electron-Driven Proton-Transfer Process. *J. Am. Chem. Soc.* **2009**, *131*, 1374–1375.

(67) Shemesh, D.; Domcke, W. Effect of the Chirality of Residues and gamma-Turns on the Electronic Excitation Spectra, Excited-State Reaction Paths and Conical Intersections of Capped Phenylalanine–Alanine Dipeptide. *ChemPhysChem* **2011**, *12*, 1833–1840.

(68) Starcke, J. H.; Wormit, M.; Dreuw, A. Unrestricted Algebraic Diagrammatic Construction Scheme of Second Order for the Calculation of Excited States of Medium-Sized and Large Molecules. *J. Chem. Phys.* **2009**, *130*, 024104.

(69) Starcke, J. H.; Wormit, M.; Dreuw, A. Nature of the Lowest Excited States of Neutral Polyenyl Radicals and Polyene Radical Cations. *J. Chem. Phys.* **2009**, *131*, 144311.

(70) Knippenberg, S.; Eisenbrandt, P.; Sistik, L.; Slavicek, P.; Dreuw, A. Simulation of Photoelectron Spectra Using the Reflection Principle in Combination with Unrestricted Excitation ADC(2) to Assess the

Accuracy of Excited-State Calculations. *ChemPhysChem* **2011**, *12*, 3180–3191.

(71) Knippenberg, S.; Rehn, D. R.; Wormit, M.; Starcke, J. H.; Rusakova, I. L.; Trofimov, A. B.; Dreuw, A. Calculations of Nonlinear Response Properties Using the Intermediate State Representation and the Algebraic-Diagrammatic Construction Polarization Propagator Approach: Two-Photon Absorption Spectra. *J. Chem. Phys.* **2012**, *136*, 064107.

(72) Thiel, W. *MNDO program*, version 6.1; Mülheim an der Ruhr: Germany, 2007.

(73) Fabiano, E.; Keal, T. W.; Thiel, W. Implementation of Surface Hopping Molecular Dynamics using Semiempirical Methods. *Chem. Phys.* **2008**, *349*, 334–347.

(74) Barbatti, M.; Granucci, G.; Persico, M.; Ruckebauer, M.; Vazdar, M.; Eckert-Maksic, M.; Lischka, H. The On-the-Fly Surface-Hopping Program System NEWTON-X: Application to ab Initio Simulation of the Nonadiabatic Photodynamics of Benchmark Systems. *J. Photochem. Photobiol., A* **2007**, *190*, 228–240.

(75) Bransden, B. H.; Joachain, C. J. *Physics of Atoms and Molecules*; Longman: New York, 1983.

(76) Tully, J. C. Molecular-Dynamics with Electronic-Transitions. *J. Chem. Phys.* **1990**, *93*, 1061–1071.

(77) Bargheer, M.; Niv, M. Y.; Gerber, R. B.; Schwentner, N. Ultrafast Solvent-Induced Spin-Flip and Nonadiabatic Coupling: CIF in Argon Solids. *Phys. Rev. Lett.* **2002**, *89*, 108301.

(78) Bargheer, M.; Cohen, A.; Gerber, R. B.; Guhr, M.; Korolkov, M. V.; Manz, J.; Niv, M. Y.; Schroder, M.; Schwentner, N. Dynamics of Electronic States and Spin-Flip for Photodissociation of Dihalogens in Matrices: Experiment and Semiclassical Surface-Hopping and Quantum Model Simulations for F-2 and CIF in Solid Ar. *J. Phys. Chem. A* **2007**, *111*, 9573–9585.

(79) Kalinowski, J.; Rasanen, M.; Gerber, R. B. Mechanism and Electronic Transition in the Cl + O<sub>3</sub> → ClO + O<sub>2</sub> Reaction: On the Fly Simulations with Multi-Reference Potentials. *Chem. Phys. Lett.* **2012**, *535*, 44–48.

(80) Bernard, Y. A.; Shao, Y. H.; Krylov, A. I. General Formulation of Spin-Flip Time-Dependent Density Functional Theory Using Non-Collinear Kernels: Theory, Implementation, and Benchmarks. *J. Chem. Phys.* **2012**, *136*, 204103.

(81) Etinski, M.; Fleig, T.; Marian, C. A. Intersystem Crossing and Characterization of Dark States in the Pyrimidine Nucleobases Uracil, Thymine, and 1-Methylthymine. *J. Phys. Chem. A* **2009**, *113*, 11809–11816.

(82) Marian, C. M. Spin–Orbit Coupling and Intersystem Crossing in Molecules. *Wiley Interdiscip. Rev.: Comput. Mol. Sci.* **2012**, *2*, 187–203.

(83) Richter, M.; Marquetand, P.; Gonzalez-Vazquez, J.; Sola, I.; Gonzalez, L. SHARC: ab Initio Molecular Dynamics with Surface Hopping in the Adiabatic Representation Including Arbitrary Couplings. *J. Chem. Theory Comput.* **2011**, *7*, 1253–1258.

(84) Marquetand, P.; Richter, M.; Gonzalez-Vazquez, J.; Sola, I.; Gonzalez, L. Nonadiabatic ab Initio Molecular Dynamics Including Spin–Orbit Coupling and Laser Fields. *Faraday Discuss.* **2011**, *153*, 261–273.

(85) Sellner, B.; Barbatti, M.; Lischka, H. Dynamics Starting at a Conical Intersection: Application to the Photochemistry of Pyrrole. *J. Chem. Phys.* **2009**, *131*, 024312.

(86) Asturiol, D.; Lasorne, B.; Worth, G. A.; Robb, M. A.; Blancafort, L. Exploring the Sloped-to-peaked S<sub>2</sub>/S<sub>1</sub> Seam of Intersection of Thymine with Electronic Structure and Direct Quantum Dynamics Calculations. *Phys. Chem. Chem. Phys.* **2010**, *12*, 4949–4958.

(87) Armstrong, D. R.; Perkins, P. G.; Stewart, J. J. P. Bond Indices and Valency. *J. Chem. Soc., Dalton Trans.* **1973**, 838–840.

(88) Hirshberg, B.; Gerber, R. B. Decomposition Mechanisms and Dynamics of N-6: Bond Orders and Partial Charges along Classical Trajectories. *Chem. Phys. Lett.* **2012**, *531*, 46–51.